Journal of Computational Physics **163,** 349–375 (2000)
doi:10.1006/jcph.2000.6571, available online at http://www.idealibrary.com on IDEAL®

A Gas-Kinetic Scheme for Multimaterial Flows and Its Application in Chemical Reactions

Y. S. Lian and K. Xu[1]

Mathematics Department, Hong Kong University of Science and Technology, Clear Water Bay, Kowloon, Hong Kong
E-mail: makxu@uxmail.ust.hk

Received July 19, 1999; revised June 9, 2000

This paper concerns the extension of the multicomponent gas-kinetic BGK-type scheme to chemical reactive flow calculations. In the kinetic model, each component satisfies its individual gas-kinetic Bhatnagar–Gross–Krook (BGK) equation, and the equilibrium states of both components are coupled in space and time due to the momentum and energy exchange in the course of particle collisions. At the same time, according to the chemical reaction rule, one component can be changed into another component with a release of energy. The reactant and product may have different ratios of specific heats. The BGK scheme basically uses the collisional Boltzmann model to mimic the numerical dissipation necessary for shock capturing. The numerical dissipation is controlled by the particle collision pseudo-time τ. In the resolved viscous calculations, there is a direct relation between the physical viscosity coefficient and the particle collision time. Many numerical test cases presented in this paper validate the gas-kinetic approach in the application of multicomponent reactive flows.

Key Words: gas-kinetic method; multicomponent flow; detonation wave.

1. INTRODUCTION

The development of numerical methods for multimaterial flows has attracted much attention in the last few years [11, 12, 21, 28]. One of the main applications of these methods is to chemical reactive flow [3, 13, 22, 25]. Research in reactive flows, especially those involving detonation waves, was pioneered by Zeldovich, von Neumann, and Doering, who developed the well-known ZND model. The ZND model consists of a nonreactive shock followed by a reaction zone. Since the model was proposed, much theoretical and numerical work on this problem has been done. Numerical calculation of the ZND detonation was pioneered by Fickett and Wood [14], who solved the one-dimensional equations using the method of

[1] To whom correspondence should be addressed. Fax: (852)2358-1643.

0021-9991/00 $35.00

characteristics in conjunction with a shock fitting method. Longitudinal instability waves were accurately simulated. Later, Taki and Fujiwara applied van Leer's upwind method to calculate two-dimensional traveling detonation waves [31, 33]. They solved the Euler equations coupled with two species equations. The chemical reaction was simulated by a two-step finite-rate model and the transverse instabilities around shock front were clearly observed. It was pointed out by Colella *et al.* in [7] that if the numerical resolution in the detonative shock front is not enough, a nonphysical solution can easily be generated. As an example, the solution may have the wrong shock speed. To avoid a nonphysical solution, Engquist and Sjögreen [9] used a high-order TVD/ENO numerical method combined with a Runge–Kutta time marching scheme to solve the combustion problem with special treatment in the shock region. Around the same time, Kailasanath *et al.* [20] extended the flux-corrected transport (FCT) algorithm for detonations. In the early 1990s, Bourlioux *et al.* combined the PPM scheme with conservative front tracking and adaptive mesh refinement in the study of detonative waves [3–5]. They computed the spatial–temporal structure of unstable detonation in one and two spatial dimensions. Quirk [27] addressed deficiency of the Godunov-type upwind schemes in solving complex flow problems and suggested a hybrid scheme to simulate the galloping phenomenon in one- and two-dimensional detonations. Recently, Short and co-workers extensively studied the nonlinear stability of a pulsating detonation wave driven by a three-step chain-branching reaction [29, 30]. Lindström [22] analyzed the poor convergence of the inviscid Euler solutions in the study of detonative waves and suggested solving the compressible Navier–Stokes equations directly. Most recently, Hwang *et al.* [17] pointed out that not only is resolution of the reaction zone important, but also the size of the computational domain is critical in capturing correct detonative solutions. So far, it is well recognized that a good scheme for reactive flow must be able to capture the correct shock speed, resolve wave structures in the multidimensional case, and determine the correct period of the possible unsteady oscillation in the wave.

Ever since the gas-kinetic scheme was proposed for the compressible flow simulations, it has attracted much attention in the CFD community due to its robustness and accuracy. The gas-kinetic schemes are usually catalogued as one group of flux vector splitting (FVS) schemes for hyperbolic equations [15, 32]. Actually, this is not completely true. For example, in the construction of numerical fluxes, the FVS scheme requires homogeneity of the governing equations, such as the Steger–Warming method for the Euler equations. But the kinetic method can be directly applied to nonhomogeneity equations, such as the shallow water equations and hyperbolic–elliptic equations [34, 36]. It can even be applied to the magnetohydrodynamic equations directly [8, 37], where an exact Riemann solution is unknown. Besides its generality, the gas-kinetic scheme distinguishes itself from other schemes by its robustness, especially for high-speed flows with shock and expansion waves. Like many other FVS schemes, the weakness of the collisionless-type kinetic methods is its overdiffusivity. It needs a much refined mesh to get an accurate Navier–Stokes solution. The reason for the overdiffusivity is the underlying free transport mechanism in the kinetic method. To improve the accuracy of the scheme, the inclusion of particle or pseudo-particle collisions becomes necessary. This leads directly to the development of the BGK scheme, where the particle collisions are included in the gas evolution process. Mathematically, from the BGK equation, the macroscopic Navier–Stokes equations can be derived [6]. In other words, for well-resolved flow simulations, the BGK flow solver and the Navier–Stokes solver yield same solutions. Actually, in this situation, any standard central difference scheme is adequate without inclusion of any upwinding or Riemann solver concept.

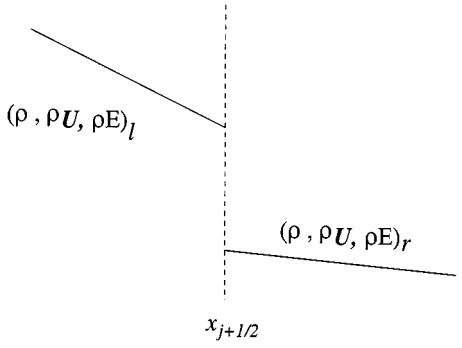

FIG. 1. The initial condition of the macroscopic flow variables used for the construction of initial gas distribution functions (10) and (11). The time dependent gas distributions evolved from the above initial data at a cell interface are presented in Eqs. (18) and (19) for different species.

However, for unresolved flow calculations, such as in inviscid flow or viscous flow with fine structure too small to be resolved by the cell size, numerical dissipation must be included. As pointed out by MacCormack [24], dissipation is the key element in numerical methodology and respect for it is paramount. The BGK scheme includes dissipation mainly by the control of the pseudo-particle collision time τ and its intrinsic collisional model. We believe that the Godunov scheme with additional viscous and heat conduction terms, gives the same result as the BGK flow solver. As presented in the current paper, the BGK scheme is based on the explicit flux function obtained from the generalized initial condition, shown in Fig. 1, and the BGK governing equation. For the Godunov method, even if a generalized Riemann solver is available [1], the viscous terms must be implemented in the solver separately by central differencing. For the multicomponent flow, the BGK-type scheme follows the time evolution of individual species, which makes it easy to implement the physical interaction between different species.

In this paper, we extend the multicomponent BGK solver [35] to higher dimensions, and we construct a scheme with the inclusion of reactive terms. The paper is organized as follows. Section 2 introduces the governing equations for chemical reactive flows in the 2D case and describes the numerical method. Section 3 discusses the numerical experiments, which include nonreactive shock bubble interaction and ZND wave calculations in both 1D and 2D cases. We also show a new example where the reactant and product could have different ratios of specific heats. Different from the previous approach [19], the current method follows the evolution of each species individually.

2. GAS-KINETIC METHOD

The focus of this section is the presentation of a kinetic scheme to solve the following reacting compressible Euler equations in the 2-D case,

$$\begin{pmatrix} \rho_1 \\ \rho_2 \\ \rho U \\ \rho V \\ \rho E \end{pmatrix}_t + \begin{pmatrix} \rho_1 U \\ \rho_2 U \\ \rho U^2 + P \\ \rho UV \\ U(\rho E + P) \end{pmatrix}_x + \begin{pmatrix} \rho_1 V \\ \rho_2 V \\ \rho UV \\ \rho V^2 + P \\ V(\rho E + P) \end{pmatrix}_y = \begin{pmatrix} -K(T)\rho_1 \\ K(T)\rho_1 \\ 0 \\ 0 \\ K(T)Q_0\rho_1 \end{pmatrix}, \qquad (1)$$

where ρ_1 is the density of the reactant, ρ_2 is the density of the product, $\rho = \rho_1 + \rho_2$ is the total density, and ρE is the total energy which includes both kinetic and thermal ones; i.e., $\rho E = \frac{1}{2}\rho(U^2 + V^2) + P_1/(\gamma_1 - 1) + P_2/(\gamma_2 - 1)$. Here U, V are the average flow velocities in the x and y directions, respectively. Each component has its specific heat ratios γ_1 and γ_2. $P = P_1 + P_2$ is the total pressure, and Q_0 is the amount of heat released per unit mass by reaction. The equation of state can be expressed as $P_1 = \rho_1 RT$ and $P_2 = \rho_2 RT$. $K(T)$ is the chemical reactive rate, which is a function of temperature. The specific form of $K(T)$ will be given in the numerical examples section.

The above reactive flow equations will be solved in two steps. In the first step, the nonreactive gas evolution parts are solved using the multimaterial gas-kinetic method. In the second step, the source terms on the right-hand side of Eq. (1) are included in the update of flow variables inside each cell.

2.1. *2-D Multicomponent BGK Scheme*

2.1.1. Gas-kinetic governing equations. The focus of this section is a multicomponent BGK scheme in two dimensions. For the two-dimensional problem, the governing equation for the time evolution of each component is the BGK model,

$$\begin{aligned} f_t^{(1)} + u f_x^{(1)} + v f_y^{(1)} &= \frac{g^{(1)} - f^{(1)}}{\tau}, \\ f_t^{(2)} + u f_x^{(2)} + v f_y^{(2)} &= \frac{g^{(2)} - f^{(2)}}{\tau}, \end{aligned} \tag{2}$$

where $f^{(1)}$ and $f^{(2)}$ are particle distribution functions for component 1 and 2 gases, and $g^{(1)}$ and $g^{(2)}$ are the corresponding equilibrium states which $f^{(1)}$ and $f^{(2)}$ approach. In the above equations, τ is the particle collision time, which determines the speed of a nonequilibrium state approaching an equilibrium one. In the BGK scheme, τ can be regarded as particle collision pseudo-time for the unresolved flow calculation; the additional dissipation provided through the control of the collision time generates artificial dissipation necessary for shock capturing. The detailed expression of τ is given in the section on numerical examples. The relations between the distribution functions and the macroscopic variables are

$$\int f^{(1)}\phi_\alpha^{(1)}\, d\Xi^{(1)} + f^{(2)}\phi_\alpha^{(2)}\, d\Xi^{(2)} = W = (\rho_1, \rho_2, \rho U, \rho V, \rho E)^T, \tag{3}$$

where

$$\begin{aligned} d\Xi^{(1)} &= du\, dv\, d\xi_1, \quad d\Xi^{(2)} = du\, dv\, d\xi_2, \\ \phi_\alpha^{(1)} &= \left(1, 0, u, v, \frac{1}{2}\left(u^2 + v^2 + \xi_1^2\right)\right)^T \\ \phi_\alpha^{(2)} &= \left(0, 1, u, v, \frac{1}{2}\left(u^2 + v^2 + \xi_2^2\right)\right)^T, \end{aligned}$$

are the moments for individual mass, total momentum, and total energy densities. Here, $\xi_1^2 = \xi_{1,1}^2 + \xi_{1,2}^2 + \cdots + \xi_{1,K_1}^2$ and $\xi_2^2 = \xi_{2,1}^2 + \xi_{2,2}^2 + \cdots + \xi_{2,K_2}^2$. The integration elements are $d\xi_1 = d\xi_{1,1}\, d\xi_{1,2} \ldots d\xi_{1,K_1}$ and $d\xi_2 = d\xi_{2,1}\, d\xi_{2,2} \ldots d\xi_{2,K_2}$. K_1 and K_2 are the degrees

of freedom of the internal variables ξ_1 and ξ_2, which are related to the specific heat ratios γ_1 and γ_2. For the two-dimensional flow, we have

$$K_1 = (5 - 3\gamma_1)/(\gamma_1 - 1) + 1 \quad \text{and} \quad K_2 = (5 - 3\gamma_2)/(\gamma_2 - 1) + 1.$$

The compatibility condition for the two-component gas mixture is

$$\int \left(g^{(1)} - f^{(1)}\right)\phi_\alpha^{(1)}\, d\Xi^{(1)} + \left(g^{(2)} - f^{(2)}\right)\phi_\alpha^{(2)}\, d\Xi^{(2)} = 0, \quad \alpha = 1, 2, 3, 4, 5. \tag{4}$$

The equilibrium Maxwellian distributions $g^{(1)}$ and $g^{(2)}$ are generally defined as

$$g^{(1)} = \rho_1(\lambda_1/\pi)^{\frac{K_1+2}{2}} e^{-\lambda_1\left((u-U_1)^2+(v-V_1)^2+\xi_1^2\right)},$$
$$g^{(2)} = \rho_2(\lambda_2/\pi)^{\frac{K_2+2}{2}} e^{-\lambda_2\left((u-U_2)^2+(v-V_2)^2+\xi_2^2\right)},$$

where λ_1 and λ_2 are functions of temperature. Due to the momentum and energy exchange in particle collisions, the equilibrium states $g^{(1)}$ and $g^{(2)}$ are assumed to have the same velocity and temperature at any point in space and time. Therefore, from the given initial macroscopic variables at any point in space and time,

$$W^{(1)} = \int g^{(1)}\phi_\alpha^{(1)}\, d\Xi^{(1)} = (\rho_1, \rho_1 U_1, \rho_1 V_1, \rho_1 E_1)^T,$$
$$W^{(2)} = \int g^{(2)}\phi_\alpha^{(2)}\, d\Xi^{(2)} = (\rho_2, \rho_2 U_2, \rho_2 V_2, \rho_2 E_2)^T,$$

we can get the corresponding equilibrium values

$$\begin{aligned} W^{(1)} &= \left(\rho_1, \rho_1 U, \rho_1 V, \frac{1}{2}\rho_1\left(U^2 + V^2 + \frac{K_1+2}{2\lambda}\right)\right)^T, \\ W^{(2)} &= \left(\rho_2, \rho_2 U, \rho_2 V, \frac{1}{2}\rho_2\left(U^2 + V^2 + \frac{K_2+2}{2\lambda}\right)\right)^T, \end{aligned} \tag{5}$$

where the equilibrium values U, V, and λ can be obtained from the mass, momentum, and energy conservation,

$$\begin{aligned} \rho &= \rho_1 + \rho_2, \\ \rho_1 U_1 + \rho_2 U_2 &= \rho U, \\ \rho_1 V_1 + \rho_2 V_2 &= \rho V, \\ \rho_1 E_1 + \rho_2 E_2 &= \frac{\rho(U^2 + V^2)}{2} + \frac{(K+2)\rho}{4\lambda}. \end{aligned} \tag{6}$$

With the definition of "averaged" value of internal degrees of freedom K,

$$K = \frac{\rho_1 K_1 + \rho_2 K_2}{\rho},$$

and the corresponding specific heat ratio γ,

$$\gamma = \frac{K+4}{K+2},$$

the values U, V, and λ can be obtained from Eq. (6) explicitly,

$$U = \frac{\rho_1 U_1 + \rho_2 U_2}{\rho},$$
$$V = \frac{\rho_1 V_1 + \rho_2 V_2}{\rho},$$

and

$$\lambda = \frac{1}{4} \frac{(K+2)\rho}{\rho_1 E_1 + \rho_2 E_2 - \frac{1}{2}\rho(U^2 + V^2)}.$$

As a result, the equilibrium states can be expressed as

$$g^{(1)} = \rho_1 (\lambda/\pi)^{\frac{K_1+2}{2}} e^{-\lambda\left((u-U)^2+(v-V)^2+\xi_1^2\right)},$$
$$g^{(2)} = \rho_2 (\lambda/\pi)^{\frac{K_2+2}{2}} e^{-\lambda\left((u-U)^2+(v-V)^2+\xi_2^2\right)}.$$

The governing equations (2) are closely related to the viscous governing equations, and the dissipative coefficients are proportional to the collision time τ [34].

2.1.2. Multicomponent gas-kinetic scheme. Numerically, the Boltzmann equations (2) are solved using a splitting method. For example, in the x direction, we solve

$$f_t^{(1)} + u f_x^{(1)} = \frac{g^{(1)} - f^{(1)}}{\tau},$$
$$f_t^{(2)} + u f_x^{(2)} = \frac{g^{(2)} - f^{(2)}}{\tau},$$

and in the y direction,

$$f_t^{(1)} + v f_y^{(1)} = \frac{g^{(1)} - f^{(1)}}{\tau},$$
$$f_t^{(2)} + v f_y^{(2)} = \frac{g^{(2)} - f^{(2)}}{\tau}.$$

In each fractional step, the compatibility condition (4) is still satisfied.

For the BGK model, in the x direction the integral solution of f at a cell interface $x_{i+1/2}$ and time t is

$$f^{(1)}\left(x_{i+1/2}, t, u, v, \xi_1\right) = \frac{1}{\tau}\int_0^t g^{(1)}(x', t', u, v, \xi_1) e^{-(t-t')/\tau}\, dt' + e^{-t/\tau} f_0^{(1)}\left(x_{i+1/2} - ut\right) \tag{7}$$

for component 1 and

$$f^{(2)}\left(x_{i+1/2}, t, u, v, \xi_2\right) = \frac{1}{\tau}\int_0^t g^{(2)}(x', t', u, v, \xi_2) e^{-(t-t')/\tau}\, dt' + e^{-t/\tau} f_0^{(2)}\left(x_{i+1/2} - ut\right) \tag{8}$$

for component 2, where $x_{i+1/2}$ is the location of the cell interface and $x' = x_{i+1/2} - u(t-t')$ is the particle trajectory. There are four unknowns in Eq. (7) and Eq. (8). Two of them are

initial gas distribution functions $f_0^{(1)}$ and $f_0^{(2)}$ at the beginning of each time step $t = 0$, and the others are $g^{(1)}$ and $g^{(2)}$ in both space and time locally around $(x_{i+1/2}, t = 0)$.

Numerically, at the beginning of each time step $t = 0$, we have the macroscopic flow distributions inside each cell i,

$$W_i = (\rho_1, \rho_2, \rho U, \rho V, \rho E)_i^T.$$

From the discretized initial data, we can apply the standard van Leer limiter $L(\cdot, \cdot)$ to interpolate the conservative variables W_i and get the reconstructed initial data

$$\bar{W}_i(x) = W_i + L(s_{i+}, s_{i-})(x - x_i), \quad \text{for } x \in \left[x_{i-1/2}, x_{i+1/2}\right], \tag{9}$$

where $(\bar{W}_i(x_{i-1/2}), \bar{W}_i(x_{i+1/2}))$ are the reconstructed point-wise values at the cell interfaces $x_{i-1/2}$ and $x_{i+1/2}$ in cell i.

To simplify the notation, in the following $x_{i+1/2} = 0$ is assumed. With the interpolated macroscopic flow distributions $\bar{W}_i$, the initial distribution functions $f_0^{(1)}$ and $f_0^{(2)}$ in Eq. (7) and Eq. (8) can be constructed as

$$f_0^{(1)} = \begin{cases} \left(1 + a_l^{(1)} x\right) g_l^{(1)}, & x < 0, \\ \left(1 + a_r^{(1)} x\right) g_r^{(1)}, & x > 0, \end{cases} \tag{10}$$

for component 1 and

$$f_0^{(2)} = \begin{cases} \left(1 + a_l^{(2)} x\right) g_l^{(2)}, & x < 0, \\ \left(1 + a_r^{(2)} x\right) g_r^{(2)}, & x > 0, \end{cases} \tag{11}$$

for component 2. The corresponding macroscopic variables for each component around the cell interface are shown in Fig. 1. The equilibrium states in Eq. (7) and Eq. (8) around $(x = 0, t = 0)$ are assumed to be

$$g^{(1)} = \left(1 + (1 - \mathrm{H}(x))\bar{a}_l^{(1)} x + \mathrm{H}(x)\bar{a}_r^{(1)} x + \bar{A}^{(1)} t\right) g_0^{(1)}, \tag{12}$$

and

$$g^{(2)} = \left(1 + (1 - \mathrm{H}(x))\bar{a}_l^{(2)} x + \mathrm{H}(x)\bar{a}_r^{(2)} x + \bar{A}^{(2)} t\right) g_0^{(2)}, \tag{13}$$

where $\mathrm{H}(x)$ is the Heaviside function. $g_0^{(1)}$ and $g_0^{(2)}$ are the initial equilibrium states located at the cell interface,

$$\begin{aligned} g_0^{(1)} &= \rho_{1,0} (\lambda_0/\pi)^{\frac{K_1+2}{2}} e^{-\lambda_0 \left((u-U_0)^2 + (v-V_0)^2 + \xi_1^2\right)}, \\ g_0^{(2)} &= \rho_{2,0} (\lambda_0/\pi)^{\frac{K_2+2}{2}} e^{-\lambda_0 \left((u-U_0)^2 + (v-V_0)^2 + \xi_2^2\right)}. \end{aligned} \tag{14}$$

The parameters $a_{l,r}^{(1,2)}$, $\bar{a}_{l,r}^{(1,2)}$, and $\bar{A}^{(1,2)}$ are from the Taylor expansion of the equilibrium states and have the forms

$$a_l^{(1,2)} = a_{l,1}^{(1,2)} + a_{l,2}^{(1,2)} u + a_{l,3}^{(1,2)} v + a_{l,4}^{(1,2)} \frac{u^2 + v^2 + \xi_{(1,2)}^2}{2},$$

$$a_r^{(1,2)} = a_{r,1}^{(1,2)} + a_{r,2}^{(1,2)} u + a_{r,3}^{(1,2)} v + a_{r,4}^{(1,2)} \frac{u^2 + v^2 + \xi_{(1,2)}^2}{2},$$

$$\bar{a}_l^{(1,2)} = \bar{a}_{l,1}^{(1,2)} + \bar{a}_{l,2}^{(1,2)} u + \bar{a}_{l,3}^{(1,2)} v + \bar{a}_{l,4}^{(1,2)} \frac{u^2 + v^2 + \xi_{(1,2)}^2}{2},$$
$$\bar{a}_r^{(1,2)} = \bar{a}_{r,1}^{(1,2)} + \bar{a}_{r,2}^{(1,2)} u + \bar{a}_{r,3}^{(1,2)} v + \bar{a}_{r,4}^{(1,2)} \frac{u^2 + v^2 + \xi_{(1,2)}^2}{2},$$
$$\bar{A}^{(1,2)} = \bar{A}_1^{(1,2)} + \bar{A}_2^{(1,2)} u + \bar{A}_3^{(1,2)} v + \bar{A}_4^{(1,2)} \frac{u^2 + v^2 + \xi_{(1,2)}^2}{2}.$$

All coefficients $a_{l,1}^{(1,2)}, a_{l,2}^{(1,2)}, \ldots, \bar{A}_4^{(1,2)}$ are local constants. To determine all these unknowns, the BGK scheme is summarized as follows.

The equilibrium Maxwellian distribution functions located on the left side of the cell interface $x_{i+1/2}$ for components 1 and 2 are

$$g_l^{(1)} = \rho_{1,l} (\lambda_l/\pi)^{\frac{K_1+2}{2}} e^{-\lambda_l \left((u-U_l)^2 + (v-V_l)^2 + \xi_1^2\right)},$$

and

$$g_l^{(2)} = \rho_{2,l} (\lambda_l/\pi)^{\frac{K_2+2}{2}} e^{-\lambda_l \left((u-U_l)^2 + (v-V_l)^2 + \xi_2^2\right)}. \tag{15}$$

At the location $x = 0$, the relations (3) and (4) require

$$\bar{W}_i\left(x_{i+1/2}\right) \equiv \begin{pmatrix} \bar{\rho}_{1,i} \\ \bar{\rho}_{2,i} \\ (\overline{\rho U})_i \\ (\overline{\rho V})_i \\ (\overline{\rho E})_i \end{pmatrix}_{x_{i+1/2}} = \int g_l^{(1)} \phi_\alpha^1 \, d\Xi^{(1)} + g_l^{(2)} \phi_\alpha^2 \, d\Xi^{(2)} = \begin{pmatrix} \rho_{1,l} \\ \rho_{2,l} \\ (\rho U)_l \\ (\rho V)_l \\ (\rho E)_l \end{pmatrix},$$

and

$$\bar{W}_{i+1}\left(x_{i+1/2}\right) \equiv \begin{pmatrix} \bar{\rho}_{1,i+1} \\ \bar{\rho}_{2,i+1} \\ (\overline{\rho U})_{i+1} \\ (\overline{\rho V})_{i+1} \\ (\overline{\rho E})_{i+1} \end{pmatrix}_{x_{i+1/2}} = \int g_r^{(1)} \phi_\alpha^{(1)} \, d\Xi^{(1)} + g_r^{(2)} \phi_\alpha^{(2)} \, d\Xi^{(2)} = \begin{pmatrix} \rho_{1,r} \\ \rho_{2,r} \\ (\rho U)_r \\ (\rho V)_r \\ (\rho E)_r \end{pmatrix},$$

from which we have

$$\begin{pmatrix} \rho_{1,l} \\ \rho_{2,l} \\ U_l \\ V_l \\ \lambda_l \end{pmatrix} = \begin{pmatrix} \bar{\rho}_{1,i} \\ \bar{\rho}_{2,i} \\ \bar{U}_i \\ \bar{V}_i \\ \frac{(K_1+2)\bar{\rho}_{1,i} + (K_2+2)\bar{\rho}_{2,i}}{4\left((\overline{\rho E})_i - \frac{1}{2}\bar{\rho}_i\left(\bar{U}_i^2 + \bar{V}_i^2\right)\right)} \end{pmatrix}_{x_{i+1/2}}.$$

Similarly,

$$\begin{pmatrix} \rho_{1,r} \\ \rho_{2,r} \\ U_r \\ V_r \\ \lambda_r \end{pmatrix} = \begin{pmatrix} \bar{\rho}_{1,i+1} \\ \bar{\rho}_{2,i+1} \\ \bar{U}_{i+1} \\ \bar{V}_{i+1} \\ \frac{(K_1+2)\bar{\rho}_{1,i+1}+(K_2+2)\bar{\rho}_{2,i+1}}{4\left((\overline{\rho E})_{i+1}-\frac{1}{2}\bar{\rho}_{i+1}\left(\bar{U}^2_{i+1}+\bar{V}^2_{i+1}\right)\right)} \end{pmatrix}_{x_{i+1/2}}.$$

Therefore, $g_l^{(1)}$, $g_l^{(2)}$, $g_r^{(1)}$, and $g_r^{(2)}$ are totally determined.

Since $g^{(1)}$ and $g^{(2)}$ have the same temperature and velocity at any point in space and time, as shown in Eq. (5), the parameters $(a_{l,1}^{(1,2)}, a_{l,2}^{(1,2)}, a_{l,3}^{(1,2)}, a_{l,4}^{(1,2)})$ are not totally independent. Since $a_{l,2}^{(1,2)}$, $a_{l,3}^{(1,2)}$, and $a_{l,4}^{(1,2)}$ depend only on derivatives of U_0, V_0, and λ_0, the requirement of common velocity and temperature in space and time gives

$$a_{l,2} \equiv a_{l,2}^{(1)} = a_{l,2}^{(2)}, \quad a_{l,3} \equiv a_{l,3}^{(1)} = a_{l,3}^{(2)}, \quad \text{and} \quad a_{l,4} \equiv a_{l,4}^{(1)} = a_{l,4}^{(2)}.$$

This is also true among the parameters $a_{r,2}^{(1)}, a_{r,2}^{(2)}, \ldots, a_{r,2}^{(1)}, a_{r,2}^{(2)}$ on the right-hand side of a cell interface. Therefore, for each cell i, we have

$$\begin{aligned} \frac{\bar{W}_i\left(x_{i+1/2}\right)-\bar{W}_i(x_i)}{x_{i+1/2}-x_i} &\equiv \begin{pmatrix} \omega_1 \\ \omega_2 \\ \omega_3 \\ \omega_4 \\ \omega_5 \end{pmatrix} \\ &= \int \left(a_{l,1}^{(1)} + a_{l,2}u + a_{l,3}v + a_{l,4}\frac{u^2+v^2+\xi_1^2}{2}\right) g_l^{(1)}\phi_\alpha^{(1)}\, d\Xi^{(1)} \\ &\quad + \left(a_{l,1}^{(2)} + a_{l,2}u + a_{l,3}v + a_{l,4}\frac{u^2+v^2+\xi_2^2}{2}\right) g_l^{(2)}\phi_\alpha^{(2)}\, d\Xi^{(2)}. \quad (16) \end{aligned}$$

The above five equations uniquely determine the five unknowns $(a_{l,1}^{(1)}, a_{l,1}^{(2)}, a_{l,2}, a_{l,3}, a_{l,4})$ and the solutions are the following: Define

$$\begin{aligned} \Pi_1 &= \omega_3 - U_l(\omega_1+\omega_2), \\ \Pi_2 &= \omega_4 - V_l(\omega_1+\omega_2), \\ \Pi_3 &= \omega_5 - \frac{U_l^2+V_l^2+\frac{K_1+2}{2\lambda_l}}{2\omega_1} - \frac{U_l^2+V_l^2+\frac{K_2+2}{2\lambda_l}}{2\omega_2}. \end{aligned}$$

The solutions of Eq. (16) are

$$\begin{aligned} a_{l,4} &= \frac{8\lambda_l^2(\Pi_3 - U_l\Pi_1 - V_l\Pi_2)}{(K_1+2)\rho_{1,l}+(K_2+2)\rho_{2,l}}, \\ a_{l,3} &= \frac{2\lambda_l}{\rho_{1,l}+\rho_{2,l}}\left(\Pi_2 - \frac{(\rho_{1,l}+\rho_{2,l})V_l}{2\lambda_l}a_{l,4}\right), \\ a_{l,2} &= \frac{2\lambda_l}{\rho_{1,l}+\rho_{2,l}}\left(\Pi_1 - \frac{(\rho_{1,l}+\rho_{2,l})U_l}{2\lambda_l}a_{l,4}\right), \end{aligned}$$

$$a_{l,1}^{(2)} = \frac{1}{\rho_{2,l}}\left(\omega_2 - \rho_{2,l}(U_l a_{l,2} + V_l a_{l,3}) - \rho_2\left(\frac{U_l^2 + V_l^2}{2} + \frac{K_2 + 2}{4\lambda_l}\right)a_{l,4}\right),$$
$$a_{l,1}^{(1)} = \frac{1}{\rho_{1,l}}\left(\omega_1 - \rho_{1,l}(U_l a_{l,2} + V_l a_{l,3}) - \rho_1\left(\frac{U_l^2 + V_l^2}{2} + \frac{K_1 + 2}{4\lambda_l}\right)a_{l,4}\right).$$

With the same method, all terms in $a_r^{(1,2)}$ terms can be obtained.

By taking the limit of $(t \to 0)$ in Eq. (7) and Eq. (8), applying the compatibility condition at $(x = x_{i+1/2}, t = 0)$, and using Eqs. (10) and (11), we get

$$\begin{aligned}
&(\rho_{1,0}, \rho_{2,0}, \rho_0 U_0, \rho_0 V_0, \rho_0 E_0)^T \\
&\quad \equiv \int g_0^{(1)}\phi_\alpha^{(1)}\, d\Xi^{(1)} + g_0^{(2)}\phi_\alpha^{(2)}\, d\Xi^{(2)} \\
&\quad = \lim_{t\to 0} e^{-t/\tau}\int f_0^{(1)}\big(x_{i+1/2} - ut\big)\phi^{(1)}\, d\Xi^{(1)} + f_0^{(2)}\big(x_{i+1/2} - ut\big)\phi^{(2)}\, d\Xi^{(2)} \\
&\quad = \int \big(\mathrm{H}(u)g_l^{(1)} + (1 - \mathrm{H}(u))g_r^{(1)}\big)\phi_\alpha^{(1)}\, d\Xi^{(1)} + \big(\mathrm{H}(u)g_l^{(2)} + (1 - \mathrm{H}(u))g_r^{(2)}\big)\phi_\alpha^{(2)}\, d\Xi^{(2)}.
\end{aligned} \tag{17}$$

The right-hand side of the above equation can be evaluated explicitly using $g_{l,r}^{(1,2)}$ in Eq. (15). Therefore, $\rho_{1,0}$, $\rho_{2,0}$, λ_0, U_0, and V_0 in Eq. (14) can be obtained by solving Eq. (17). As a result, $g_0^{(1)}$ and $g_0^{(2)}$ are determined. Then, connecting the macroscopic variables

$$W_0 = (\rho_{1,0}, \rho_{2,0}, \rho_0 U_0, \rho_0 V_0, \rho_0 E_0)^T$$

at the cell interface with the cell-centered values in Eq. (9) on both sides, we get the slopes for the macroscopic variables,

$$\frac{W_0 - \bar{W}_i(x_i)}{x_{i+1/2} - x_i}, \quad \text{and} \quad \frac{\bar{W}_{i+1}(x_{i+1}) - W_0}{x_{i+1} - x_{i+1/2}},$$

from which $\bar{a}_l^{(1)}$ and $\bar{a}_l^{(1)}$ in Eq. (12) and $\bar{a}_r^{(2)}$ and $\bar{a}_r^{(2)}$ in Eq. (13) can be determined using the same techniques for solving Eq. (16). At this point, there are only two unknowns $\bar{A}^{(1,2)}$ left for the time evolution parts of the gas distribution functions in Eq. (12) and Eq. (13).

Substituting Eq. (10), Eq. (11), Eq. (12), and Eq. (13) into the integral solutions Eq. (7) and Eq. (8), we get

$$\begin{aligned}
f^{(1)}\big(x_{i+1/2}, t, u, v, \xi_1\big) = {} & \big(1 - e^{-t/\tau}\big)g_0^{(1)} + \tau\big(t/\tau - 1 + e^{-t/\tau}\big)\bar{A}^{(1)}g_0^{(1)} \\
& + \big(\tau\big(-1 + e^{-t/\tau}\big) + te^{-t/\tau}\big)\big(\bar{a}_l^{(1)}\mathrm{H}(u) + \bar{a}_r^{(1)}(1 - \mathrm{H}(u))\big)ug_0^{(1)} \\
& + e^{-t/\tau}\big(\big(1 - uta_l^{(1)}\big)\mathrm{H}(u)g_l^{(1)} + \big(1 - uta_r^{(1)}\big)(1 - \mathrm{H}(u))g_r^{(1)}\big),
\end{aligned} \tag{18}$$

and

$$\begin{aligned}
f^{(2)}\big(x_{i+1/2}, t, u, v, \xi_2\big) = {} & \big(1 - e^{-t/\tau}\big)g_0^{(2)} + \tau\big(t/\tau - 1 + e^{-t/\tau}\big)\bar{A}^{(2)}g_0^{(2)} \\
& + \big(\tau\big(-1 + e^{-t/\tau}\big) + te^{-t/\tau}\big)\big(\bar{a}_l^{(2)}\mathrm{H}[u] + \bar{a}_r^{(2)}(1 - \mathrm{H}(u))\big)ug_0^{(2)} \\
& + e^{-t/\tau}\big(\big(1 - uta_l^{(2)}\big)\mathrm{H}(u)g_l^{(2)} + \big(1 - uta_r^{(2)}\big)(1 - \mathrm{H}(u))g_r^{(2)}\big).
\end{aligned} \tag{19}$$

To evaluate the unknowns $\bar{A}^{(1,2)}$ in the above two equations, we can use the compatibility condition at the cell interface $x_{i+1/2}$ over the whole CFL time step Δt,

$$\int_0^{\Delta t}\int \left(g^{(1)} - f^{(1)}\right)\phi_\alpha^{(1)}\, d\Xi^{(1)}\, dt + \left(g^{(2)} - f^{(2)}\right)\phi_\alpha^{(2)}\, d\Xi^{(2)}\, dt = 0,$$

from which we can get

$$\begin{aligned}
&\int g_0^{(1)}\bar{A}^{(1)}\phi_\alpha^{(1)}\, d\Xi^{(1)} + g_0^{(2)}\bar{A}^{(2)}\phi_\alpha^{(2)}\, d\Xi^{(2)} \\
&\quad = \int \left(\bar{A}_1^{(1)} + \bar{A}_2 u + \bar{A}_3 v + \bar{A}_4\frac{u^2+v^2+\xi_1^2}{2}\right) g_0^{(1)}\phi_\alpha^{(1)}\, d\Xi^{(1)} \\
&\qquad + \left(\bar{A}_1^{(2)} + \bar{A}_2 u + \bar{A}_3 v + \bar{A}_4\frac{u^2+v^2+\xi_2^2}{2}\right) g_0^{(2)}\phi_\alpha^{(2)}\, d\Xi^{(2)} \\
&\quad = \frac{1}{\gamma_0}\int \left[\gamma_1 g_0^{(1)} + \gamma_2 u\left(\bar{a}_l^{(1)}\mathrm{H}(u) + \bar{a}_r^{(1)}(1-\mathrm{H}(u))\right) g_0^{(1)} + \gamma_3\left(\mathrm{H}(u)g_l^{(1)} + (1-\mathrm{H}(u))g_r^{(1)}\right)\right. \\
&\qquad \left. + \gamma_4 u\left(a_l^{(1)}\mathrm{H}(u)g_l^{(1)} + a_r^{(1)}(1-\mathrm{H}(u))g_r^{(1)}\right)\right]\phi_\alpha^{(1)}\, d\Xi^{(1)} + \left[\gamma_1 g_0^{(2)} + \gamma_2 u\left(\bar{a}_l^{(2)}\mathrm{H}(u)\right.\right. \\
&\qquad \left.\left. + \bar{a}_r^{(2)}(1-\mathrm{H}(u))\right) g_0^{(2)} + \gamma_3\left(\mathrm{H}(u)g_l^{(2)} + (1-\mathrm{H}(u))g_r^{(2)}\right) + \gamma_4 u\left(a_l^{(2)}\mathrm{H}(u)g_l^{(2)}\right.\right. \\
&\qquad \left.\left. + a_r^{(2)}(1-\mathrm{H}(u))g_r^{(2)}\right)\right]\phi_\alpha^{(2)}\, d\Xi^{(2)}, \qquad (20)
\end{aligned}$$

where

$$\begin{aligned}
\gamma_0 &= \Delta t - \tau\left(1 - e^{-\Delta t/\tau}\right), \\
\gamma_1 &= -\left(1 - e^{-\Delta t/\tau}\right), \\
\gamma_2 &= -\Delta t + 2\tau\left(1 - e^{-\Delta t/\tau}\right) - \Delta t e^{-\Delta t/\tau}, \\
\gamma_3 &= \left(1 - e^{-\Delta t/\tau}\right),
\end{aligned}$$

and

$$\gamma_4 = -\tau\left(1 - e^{-\Delta t/\tau}\right) + \Delta t e^{-\Delta t/\tau}.$$

The right-hand side of Eq. (20) is known; therefore all parameters in $\bar{A}^{(1,2)}$ terms can be obtained explicitly.

Finally the time-dependent numerical fluxes for component 1 and component 2 gases across a cell interface can be obtained by taking the moments of the individual gas distribution functions $f^{(1)}$ and $f^{(2)}$ in Eq. (18) and Eq. (19) separately, which are

$$\begin{pmatrix} \mathcal{F}_{\rho_1} \\ 0 \\ \mathcal{F}_{\rho_1 U_1} \\ \mathcal{F}_{\rho_1 V_1} \\ \mathcal{F}_{\rho_1 E_1} \end{pmatrix}_{i+1/2} = \int u\phi_\alpha^{(1)} f^{(1)}\left(x_{i+1/2}, t, u, v, \xi_1\right) d\Xi^{(1)},$$

and

$$\begin{pmatrix} 0 \\ \mathcal{F}_{\rho_2} \\ \mathcal{F}_{\rho_2 U_2} \\ \mathcal{F}_{\rho_2 V_2} \\ \mathcal{F}_{\rho_2 E_2} \end{pmatrix}_{i+1/2} = \int u \phi_\alpha^{(2)} f^{(2)}\left(x_{i+1/2}, t, u, v, \xi_2\right) d\Xi^{(2)}.$$

Integrating the above time-dependent flux functions in a whole time step Δt, we can get the total mass, momentum, and energy transports for each component, from which the flow variables in each cell can be updated.

In comparison with traditional central schemes and popular Riemann solvers, the evaluation of the gas distributions in Eqs. (18) and (19) is relatively expensive. However, both the viscous effect and the coupling of the spatial and temporal gas evolution are included in these distribution functions. Therefore, in a certain sense, the BGK method gives a more accurate representation of the flow motion under a more generalized initial condition, i.e., the inclusion of slopes at the left- and right-hand sides of a cell interface; see Fig. 1. If only inviscid flux functions are required, the distribution functions can be simplified to

$$f^{(1)}\left(x_{i+1/2}, t, u, v, \xi_1\right) = \left(1 - e^{-t/\tau}\right) g_0^{(1)} + e^{-t/\tau}\left(\mathrm{H}(u) g_l^{(1)} + (1 - \mathrm{H}(u)) g_r^{(1)}\right),$$

and

$$f^{(2)}\left(x_{i+1/2}, t, u, v, \xi_1\right) = \left(1 - e^{-t/\tau}\right) g_0^{(2)} + e^{-t/\tau}\left(\mathrm{H}(u) g_l^{(2)} + (1 - \mathrm{H}(u)) g_r^{(2)}\right).$$

This simplified formulation has been applied to the MHD simulation [37].

2.2. *Reaction Step and Flow Update*

After obtaining the flux functions across a cell interface, we need to solve an ODE to account for the source term, i.e., $W_t = S$. More specifically, inside each cell we need to solve

$$\begin{cases} (\rho_1)_t = -K(T)\rho_1, \\ (\rho_2)_t = K(T)\rho_1, \\ (\rho E)_t = K Q_0 \rho_1. \end{cases} \tag{21}$$

In the current study, one step forward-Euler method is used to solve the above equations.

In summary, the update of the flow variables inside cell (i, j) from step n to $n+1$ is through the formulation

$$W_{i,j}^{n+1} = W_{i,j}^n + \frac{1}{\Delta V}\left(\Delta y \int_0^{\Delta t} \left(F_{i-1/2,j} - F_{i+1/2,j}\right) dt + \Delta x \int_0^{\Delta t} \left(G_{i,j-1/2} - G_{i,j+1/2}\right) dt\right) + \Delta t S_{i,j},$$

where $S_{i,j}$ is the corresponding source term in cell (i, j), F and G are numerical fluxes across cell interfaces by solving the multicomponent BGK equations, and ΔV is the area of the cell (i, j). We have also tried a second-order Runge–Kutta time stepping method to update

the source term. It is observed that there is basically no difference in the simulation results between using first- and second-order time stepping schemes for the test cases presented in the next section.

3. NUMERICAL EXAMPLES

In this section, we test the multicomponent BGK scheme for both nonreactive and reactive flows. For the viscous calculations, the collision time τ in the BGK scheme presented in the last section is set to be

$$\tau = \mu / P,$$

where μ is the dynamical viscosity coefficient and P is the total local pressure. For the viscous flow, μ is a fixed number. In the mesh-refinement study of the viscous flow calculation, the simulation results can be convergent only after the physical viscosity takes a dominant role and the physical structure can be well resolved by the mesh size. The convergence study of the BGK scheme for the Rayleigh–Taylor case is presented in [19]. The kinetic BGK method is actually a mesoscopic model rather than a microscopic model for the flow description. The collision time τ cannot take the real particle collision time, such as 10^{-9} s for the molecular collisions in the air, because it is impossible to get such a refined mesh size and time step to resolve individual particle collision. In the BGK scheme for the Navier–Stokes solution, the collision time is solely determined from the macroscopic viscosity coefficient.

For the inviscid flow calculations, the collision time is defined as

$$\tau = 0.05\Delta t + \frac{|P_l - P_r|}{P_l + P_r}\Delta t,$$

where Δt is the CFL time step, and P_l and P_r are the corresponding pressure in the states g_l and g_r of the initial gas distribution function f_0. With the above definition, the numerical dissipation will be reduced along with the mesh refinement. In the smooth flow region, the above expression gives about 20 collisions inside each time step. In other words, the magnitude of corresponding numerical diffusion is about $1/10$ of that in the kinetic flux vector splitting (KFVS) scheme [23, 26, 34]. In the discontinuous region, the collision time will be close to the time step in order to provide enough dissipation to construct a numerical discontinuity jump. Whatever the collision time, numerical dissipation always exist in the BGK scheme and is consistent with the Navier–Stokes dissipative terms. In other words, the BGK scheme gives an approximate solution under the generalized initial condition (Fig. 1) for the viscous governing equations, and the viscosity coefficient is controlled by the particle collision pseudo-time. Starting from the Godunov method, it is equivalent to construct a generalized Riemann solution for the viscous governing equations. Also, the current approach is more robust than the previous "single component" kinetic method for the reactive flows [19]. The detail comparison is given in [18].

For the chemical reactive flow, if the flow structure is not well resolved by the mesh size, the current BGK scheme cannot get grid-independent solutions. It is true for any other shock capturing scheme applied to the reactive flows. As realized by Lindstorm [22], to obtain grid-independent solutions, a large amount of physical viscosity must be added in the flow simulations. The BGK scheme does it through the inclusion of large collision time, such as the case (5) in the reactive flow calculation section.

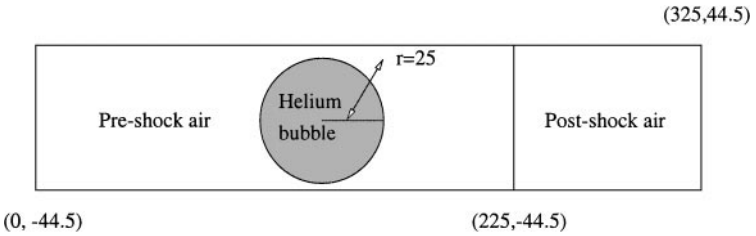

FIG. 2. Physical domain for shock–bubble interaction.

3.1. *Nonreactive Multimaterial Flow Calculations*

In this section, we show two cases of shock–bubble interactions. The main differences between these two cases are the specific heat ratios and the initial gas densities inside the bubble with respect to the density of the outside air. The density difference yields different flow patterns around the material interface after its interaction with the shock.

Case (1): A M_s =1.22 shock wave in air hits a helium cylindrical bubble. We examine the interaction of a $M_s = 1.22$ planar shock wave, moving in the air, with a cylindrical helium bubble. Experimental data can be found in [16] and numerical solutions using adaptive mesh refinement have been reported in [28]. Recently, a ghost fluid method has been applied to this case too [11]. A schematic description of the computational setup is shown in Fig. 2, where reflection boundary conditions are used on the upper and lower boundaries. The initial flow distribution is determined from the standard shock relation with the given strength of the incident shock wave. The bubble is assumed to be in both thermal and mechanical equilibrium with the surrounding air. The nondimensionalized initial conditions are

$$W = (\rho = 1, U = 0, V = 0, P = 1, \gamma = 1.4) \quad \text{preshock air}$$
$$W = (\rho = 1.3764, U = -0.394, V = 0, P = 1.5698, \gamma = 1.4) \quad \text{postshock air}$$
$$W = (\rho = 0.1358, U = 0, V = 0, P = 1, \gamma = 1.67) \quad \text{helium.}$$

The nondimensional cell size used in the computation is $\Delta x = \Delta y = 0.25$.

To identify weak flow features which are often lost within contour plots, we present a number of numerical Schlieren images. These pictures depict the magnitude of the gradient of the density field

$$|\Delta\rho| = \sqrt{\left(\frac{\partial\rho}{\partial x}\right)^2 + \left(\frac{\partial\rho}{\partial y}\right)^2}, \tag{22}$$

and hence they may be viewed as idealized images; the darker the image, the larger the gradient. The density derivatives are computed using straightforward central-differencing. The following nonlinear shading function ϕ is used to accentuate weak flow features [28],

$$\phi = \exp\left(-k\frac{|\Delta\rho|}{|\Delta\rho|_{max}}\right), \tag{23}$$

where k is a constant which takes the value 10 for helium and 60 for air. For the Refrigerant 22 (R22) simulation in the next test case, we use 1 for heavy fluid and 80 for air.

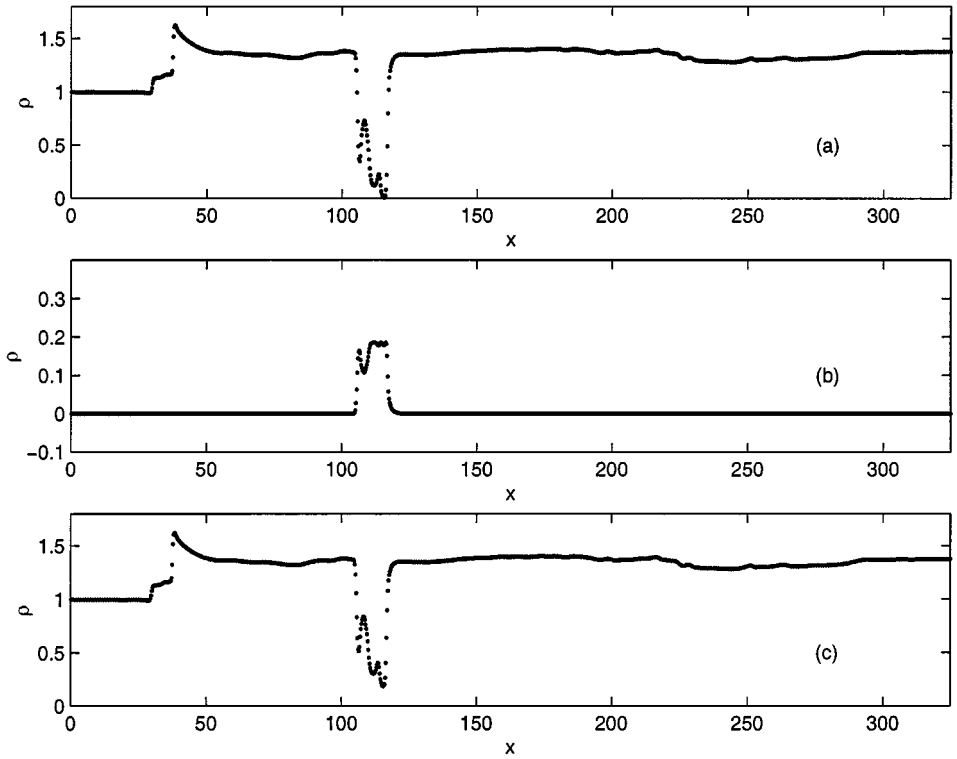

FIG. 4. The density profiles along the centerline for the shock-Helium interaction case at time $t = 125.0$. (a) Density of air, (b) density of Helium, and (c) total density.

Figure 3 shows snapshots of numerical Schlieren-type images at nondimensional times $t = 0.0$ and $t = 125.0$. Before the shock hits the bubble, wiggles usually appear around the bubble because the numerical scheme cannot precisely keep the sharp material interface. The wiggles spread in all directions. When they reach the solid wall, they bounce back. But all these noises have a very small magnitude. After the shock hits the bubble, the original shock wave separates into a reflected and a transmitted shock wave. A complex pattern of discontinuities has formed around the top and bottom of the bubble. Figure 4 shows the density distributions around the central line at time $t = 125.0$. There are approximately 10 points around the material interface, which is much wider than those obtained from schemes with special treatment at the material interfaces [11, 21]. In other words, the kinetic scheme always has an intrinsic dissipative term, and it is impossible to keep a very sharp interface. A similar phenomenon takes place in the 1D case [1]. Since helium has a lower density than air, any small perturbation at the material interface can be amplified to form the interface instability. This instability at the material interface is closely related to the Richtmyer–Meshkov instability. In comparison with the result in [11], the current scheme could capture the unstable interface structure automatically, and the result here is qualitatively consistent with both the experiment and that from the mesh-refinement study [28]. It is a common practice that many schemes with special treatments at the material interface could easily remove the interface instability. So, it is an interesting problem to further study the shock–bubble interaction case and to understand the dynamics of any special numerical treatment on the interface stability. In our calculations, the stable and unstable interfaces are captured automatically.

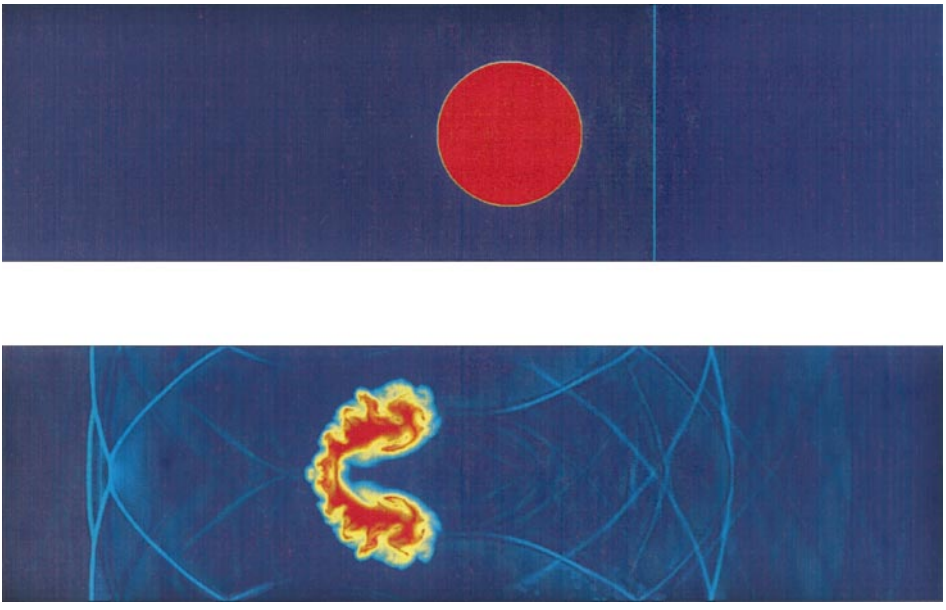

FIG. 3. Numerical Schlieren images of the interaction between a $M_s = 1.22$ shock wave in the air and a helium cylindrical bubble. The shock is moving from right to left. The second image describes the fields of the density gradient distribution at time $t = 125.0$, where the red corresponds to one material and the blue to another one.

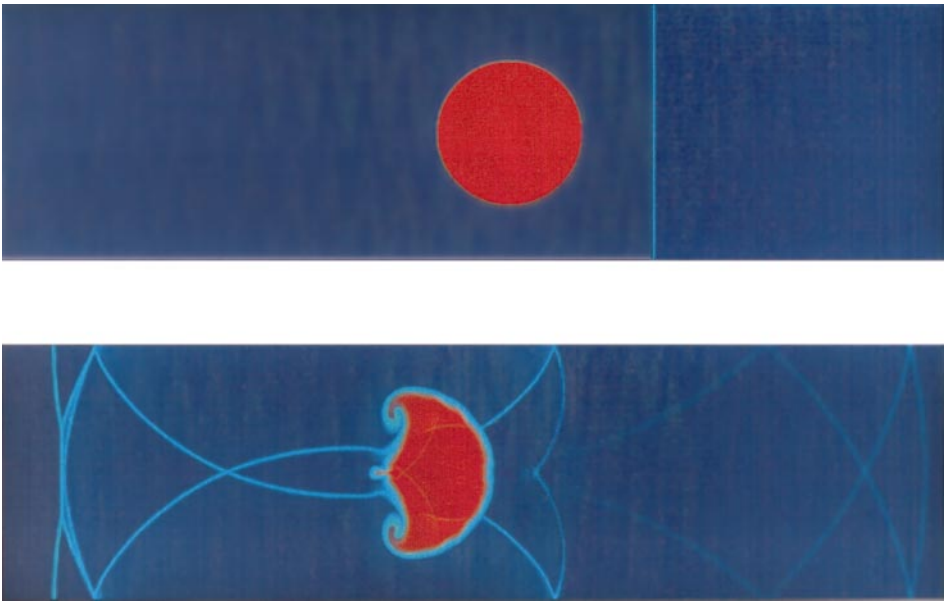

FIG. 5. Numerical Schlieren images of the interaction between a $M_s = 1.22$ shock wave and a R22 cylindrical bubble. The second image describes the fields of the density gradient distribution at time $t = 150.0$, where the red color represents one material and the blue color another one.

Case (2): A $M_s = 1.22$ shock wave hits a R22 cylindrical bubble. With the same scheme, we investigate the interaction of a $M_s = 1.22$ planar shock wave moving in the air impinging upon a R22 cylindrical bubble. The main difference between this case and the previous one is that the density of the bubble here is much heavier than the density of air. The initial data are

$$W = (\rho = 1, U = 0, V = 0, P = 1, \gamma = 1.4) \quad \text{preshock air}$$

$$W = (\rho = 1.3764, U = -0.394, V = 0, P = 1.5698, \gamma = 1.4) \quad \text{postshock air}$$

$$W = (\rho = 3.1538, U = 0, V = 0, P = 1, \gamma = 1.249) \quad \text{R22}.$$

In the numerical experiment we use $\Delta x = \Delta y = 0.25$. Figure 5 shows two snapshots of numerical Schlieren-type images at nondimensional times $t = 0.0$ and $t = 150.0$. Figure 6 presents the density distributions along the symmetric line. Due to the higher density in the bubble region, the material interface in this case is basically stable. Again, this result is qualitatively consistent with our physical understanding.

3.2. *Reactive Flow Calculations*

The study of detonation waves has been undertaken theoretically and computationally for over a century. The successful theory of Zel'dovich, von Neumann, and Doering has come

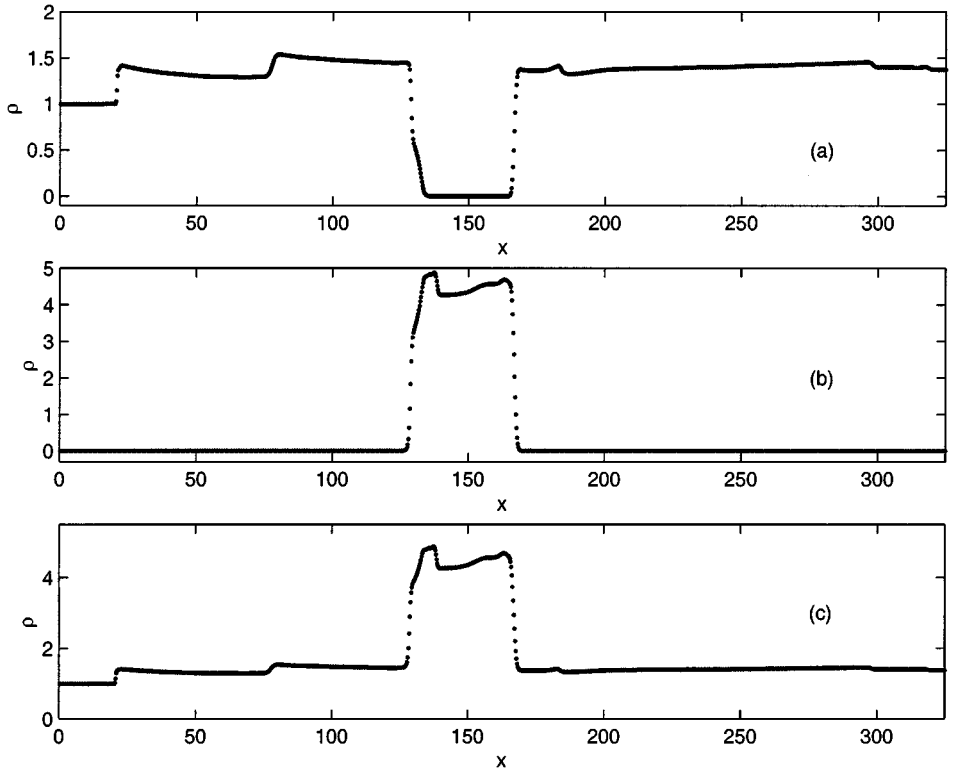

FIG. 6. The density profiles along the centerline for the shock–R22 interaction case at time $t = 150.0$. (a) Density of air, (b) density of R22, and (c) total density.

to be a standard model. The ZND solution for the reacting compressing Euler equations is described in [13]. It consists of a nonreactive shock followed by a reaction zone; both the shock and the reaction zone travel at a constant speed D. Given the specific heat ratio γ and the heat release Q_0, there is a minimum shock speed, the so-called Chapman–Jouguet value, D_{CJ}, above which the ZND solution can be constructed.

The parameter that relates the shock speed D of a given detonation wave to the CJ velocity D_{CJ} is the overdrive factor f, which is defined as

$$f \equiv \left(\frac{D}{D_{CJ}}\right)^2. \tag{24}$$

The value of f is one of the factors that determine the stability of the detonative front.

In the following test cases, we only consider reactive flows with two species, i.e., a reactant and a product. The reactant is converted to the product by a one-step irreversible reactive rule governed by Arrhenius kinetics. The factor $K(T)$, which depends on the temperature, is given by

$$K(T) = K_0 T^{\alpha} e^{-E^+/T},$$

where K_0 is a positive constant and E^+ is the activation energy. In the current paper, we assume that $\alpha = 0$ and the gas constant R is normalized to unity. Therefore, the above temperature T is determined by $T = P/\rho$.

One important parameter in the numerical calculation of ZND solution is the half-reaction length $L_{1/2}$, which is defined as the distance for half-completion of the reactant starting from the shock front. Usually the reaction prefactor K_0 is selected so that the half-reaction length is unity. From the Arrhenius formula, the half-reaction length is defined as

$$L_{1/2} = \int_1^{1/2} \frac{D-U}{K_0 Z \exp(-E^+/T)}\, dZ, \tag{25}$$

where D is the speed of the shock, and U is the postshock flow speed.

In the output of numerical results, the mass fraction Z is defined as

$$Z = \frac{\rho_1}{\rho_1 + \rho_2}.$$

Case (1): 1-D stable ZND detonation: $\gamma = 1.2$, $Q_0 = 50$, $E^+ = 50.0$, $f = 1.8$. This test case is from [3]. The preshock state is normalized to $P_0 = \rho_0 = 1$ and velocity $U_0 = V_0 = 0$, and the postshock can be obtained using the Chapman–Jouguet condition. The prefactor K_0 is chosen to be $K_0 = 145.68913$ so that the length of the half-reaction zone $L_{1/2}$ is unity. This case corresponds to the stable ZND profile. The results with 10, 20, and 40 points/$L_{1/2}$ are shown in Figs. 7 and 8.

Case (2): 1-D unstable detonation: $\gamma = 1.2$, $Q_0 = 50$, $E^+ = 50$, $f = 1.6$. To obtain a high-quality simulation result for the unstable overdriven detonation, a high-resolution solution is usually required to resolve the instability. At the same time, the correct capturing of oscillatory period requires a large computational domain. As pointed out in [17], for a particular computation, one may be tempted to keep only a few points behind the shock, with the reasoning that the information behind the shock either never catches up with or

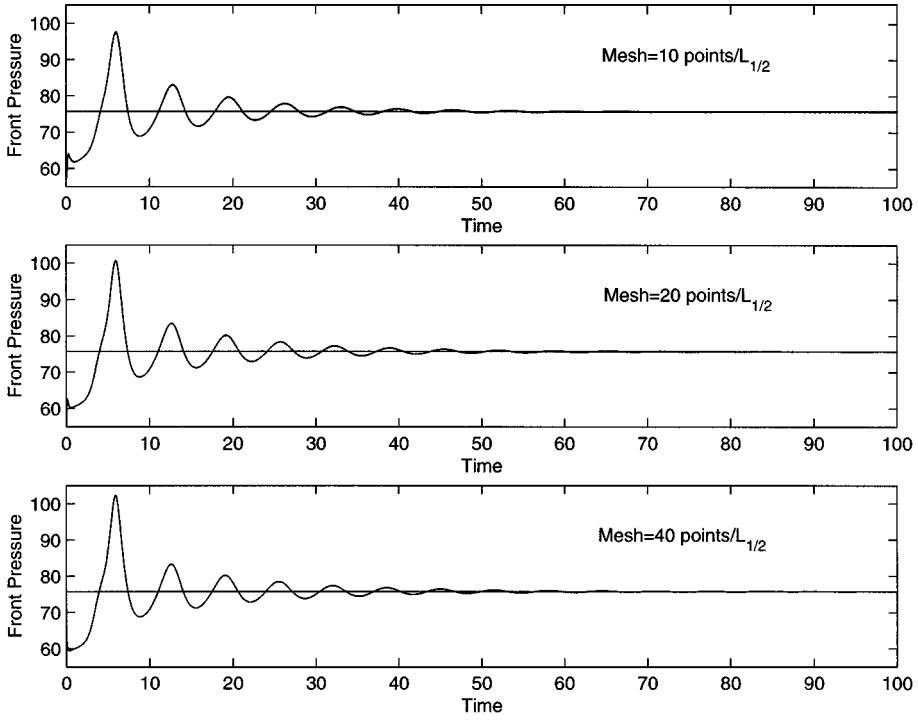

FIG. 7. Mesh refinement study of the pressure history at the shock front for the stable detonation wave, where $f = 1.8$, $\gamma = 1.2$, $Q_0 = E^+ = 50$, and $L_{1/2} = 1.0$ (CFL $= 0.5$).

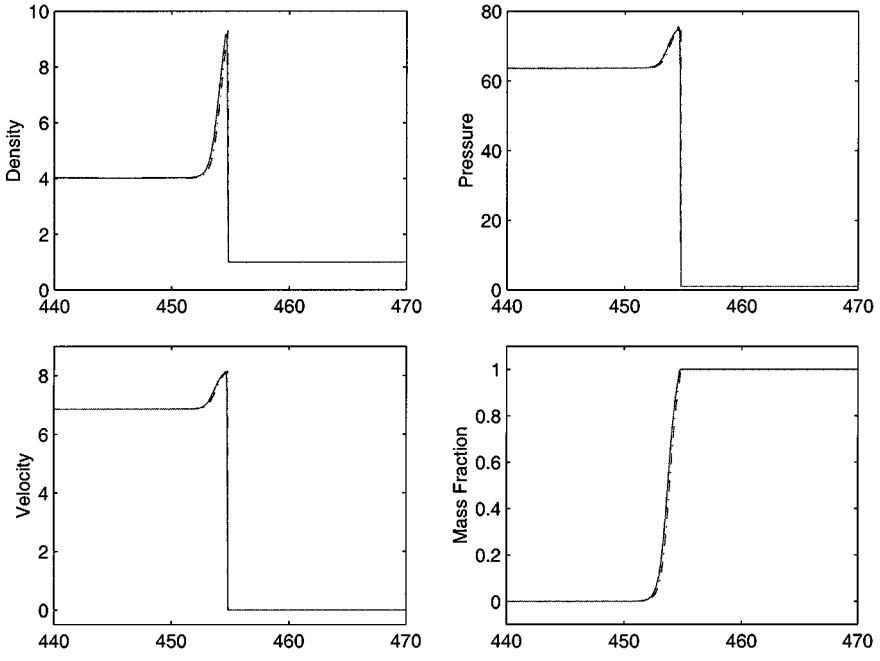

FIG. 8. Numerical solutions (solid lines) of density ρ, velocity U, pressure P and mass fraction Z, where $f = 1.8$, $\gamma = 1.2$, $Q_0 = E^+ = 50$, $L_{1/2} = 1.0$, and 10 points/$L_{1/2}$ (CFL $= 0.5$). The dash lines are the exact solutions.

does not affect the shock during the computation. However, if too small a computational domain behind the shock is specified, the points at the edge of and outside the computational domain cease to be updated after some time, leading to corruption of the data in that region. The $U + c$ waves emanating from an inappropriate boundary condition eventually catch up with the shock itself and alter the shock properties erroneously. The analysis in [17] shows that if one expects the numerical results at time t to be correct, the computational domain L and t must satisfy the inequality

$$t < \frac{L}{U + c - D} + \frac{L}{D}, \tag{26}$$

where U is the speed of the postshock flow, and c is the sound speed. For the current test, L should satisfy

$$L \geq 1.88t.$$

This classical unstable detonation wave was first studied by Fickett and Wood [14]. An important physical quality for unstable detonation is the pressure history at the precursor shock in the oscillatory ZND wave as a function of time. For a stable ZND wave, this shock pressure history should exhibit small fluctuations about the known precursor shock value and decay as time evolves. In the case of unstable detonations, the shock front pressure history makes larger excursions from the ZND value. For the case $\gamma = 1.2$, $q_0 = 50$, $E^+ = 50$, and overdrive $f = 1.6$, according to Erpenbeck [10] this ZND profile is a regular periodic pulsating detonation with a maximum shock pressure given by 101.1 ± 0.2 while the unperturbed ZND shock pressure is 67.3.

In the current study, the density and pressure are normalized to unity after the shock. Since $Q_0 = 50$, $\gamma = 1.2$, the CJ speed becomes $D_{CJ} = 6.80947$, and the prefactor is chosen to be $K_0 = 230.75$ to get a unit half-reaction length. The postshock state can be determined by the Chapman–Jouguet condition with the given shock speed. Due to the "start-up" numerical incompatibility, there is a large initial shock pressure up to 114 at time t equal to 8; see Fig. 9. After $t > 15$, the motion of the shock front becomes periodic.

In this test, we observe that at least 20 points/$L_{1/2}$ are needed for a correct unstable ZND solution. In Figs. 9 and 10 we show the numerical results with 20 points/$L_{1/2}$ and 40 points/$L_{1/2}$, respectively. At the same time, the result with 80 points/$L_{1/2}$ is given as a reference. In Table I, the data of local maximum and minimum pressure as a function of time are listed.

Case (3): Weak shock wave hitting the reactant. To validate the multicomponent BGK scheme, we design the following 1D case to simulate the chemical reaction in which the reactant and product have different specific heat ratios γ. The initial condition is

$$W_L = (\rho_L, U_L, P_L, \gamma_L) = (2.667, 1.479, 4.500, 1.4) \quad \text{postshock air}$$
$$W_M = (\rho_M, U_M, P_M, \gamma_M) = (1.0, 0.0, 1.0, 1.4) \quad \text{preshock air}$$
$$W_R = (\rho_R, U_R, P_R, \gamma_R) = (0.287, 0.0, 1.0, 1.2) \quad \text{(reactant)}.$$

This is a case of a weak shock wave with $M = 2.0$ hitting the reactant. We use the Arrhenius form for the reaction rate with $E^+ = Q_0 = 50$ and $K_0 = 600.0$. The numerical cell size is

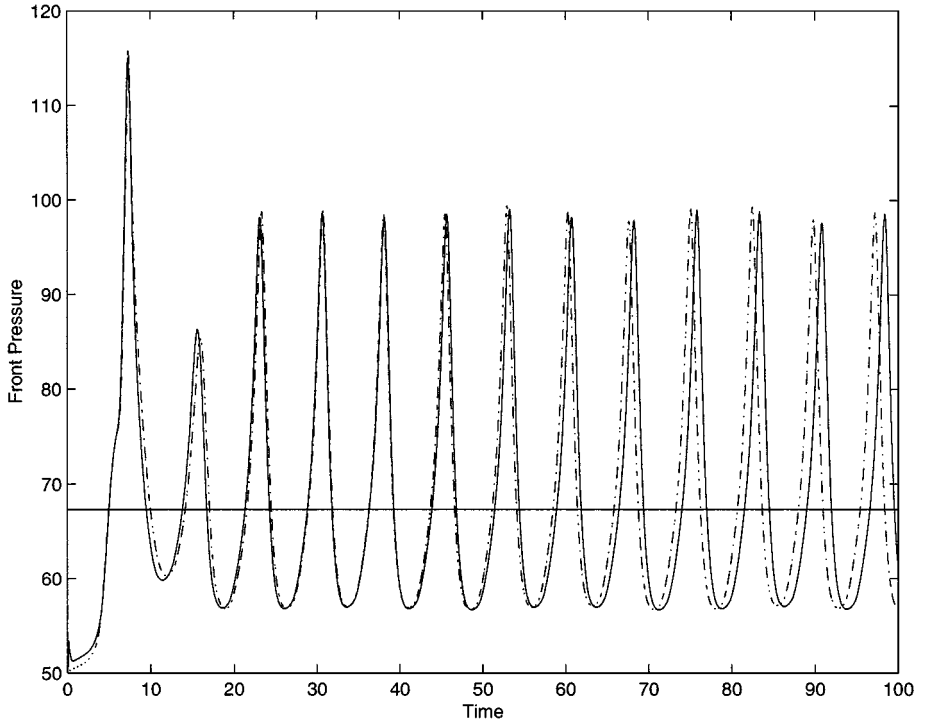

FIG. 9. Local maximum pressure variation as a function of time for the overdriven detonation, where $f = 1.6$, $\gamma = 1.2$, $Q_0 = E^+ = 50$, and $L_{1/2} = 1.0$. Solid line, 80 points/$L_{1/2}$, and dash-dot line, 20 points/$L_{1/2}$ (CFL $= 0.5$).

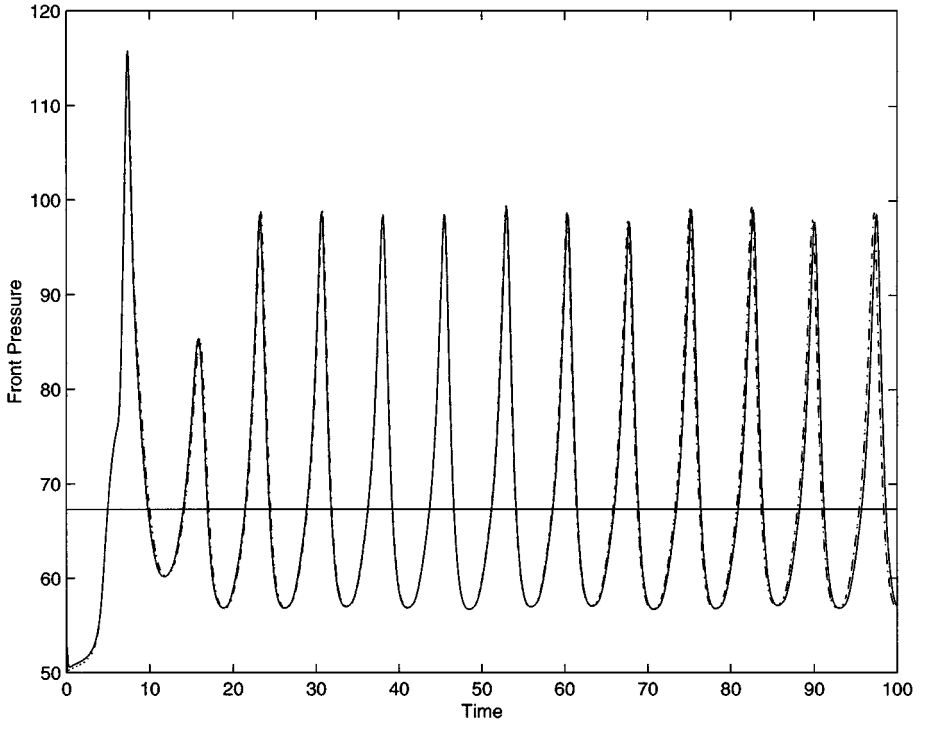

FIG. 10. Local maximum pressure variation as a function of time for the overdriven detonation, where $f = 1.6$, $\gamma = 1.2$, $Q_0 = E^+ = 50$, and $L_{1/2} = 1.0$. Solid line, 80 points/$L_{1/2}$, dash-dot line, 40 points/$L_{1/2}$ (CFL $= 0.5$).

TABLE I

Maximum and Minimum Pressure vs Time for $f = 1.6$ and $80/L_{1/2}$

Time	Maximum	Time	Minimum
7.3513	114.1553	11.8038	60.1576
15.9353	85.0627	18.9221	56.7383
23.3201	98.1318	26.3057	56.7478
30.7833	98.3344	33.6993	56.8976
38.1373	97.8645	41.1103	56.7854
45.6102	98.0387	48.6158	56.5972
53.1075	98.8378	56.0587	56.8738
60.5059	98.1242	63.4607	56.9737
67.9318	97.3600	70.8918	56.6064
75.4233	98.6184	78.3885	56.6841
82.8773	98.7023	85.8014	57.0227
90.2201	97.3901	93.2212	56.7298
97.6928	98.2211		

$\Delta x = 1/2000$. Figure 11 shows the numerical results at time $t = 0.20$. Since the shock is too weak to construct a ZND wave, the solution is the same as the shock hits the nonreactive two-component flow interface. There is a transmitted shock moving forward and a rarefaction wave moving backward.

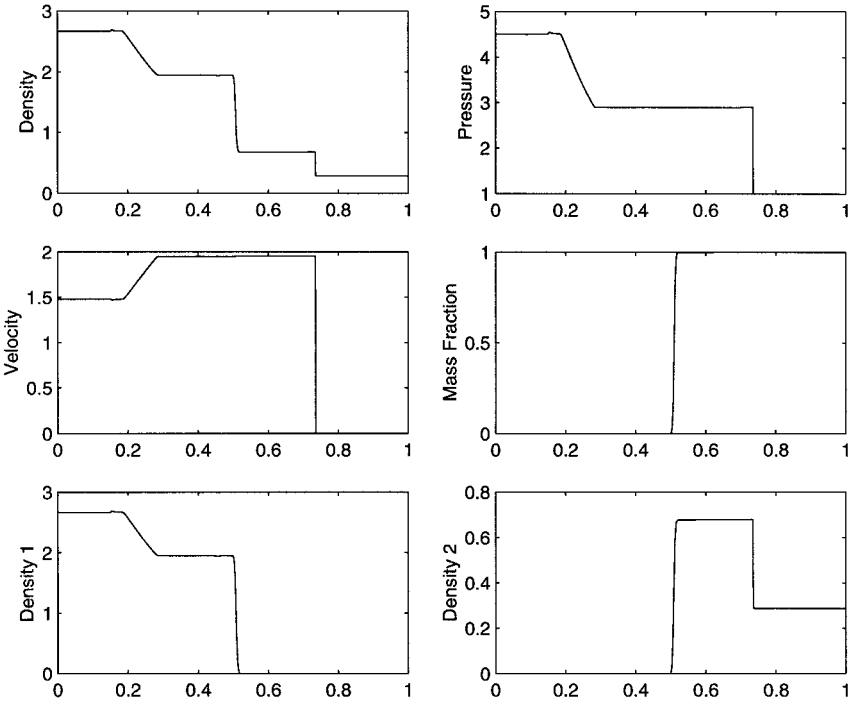

FIG. 11. Weak shock wave ($M = 2.0$) in the air ($\gamma = 1.4$) hits the reactant gas ($\gamma = 1.2$). The cell size is $\Delta x = 1/2000$. The reaction has $E^+ = Q_0 = 50$, and $K_0 = 600.0$ (CFL $= 0.5$).

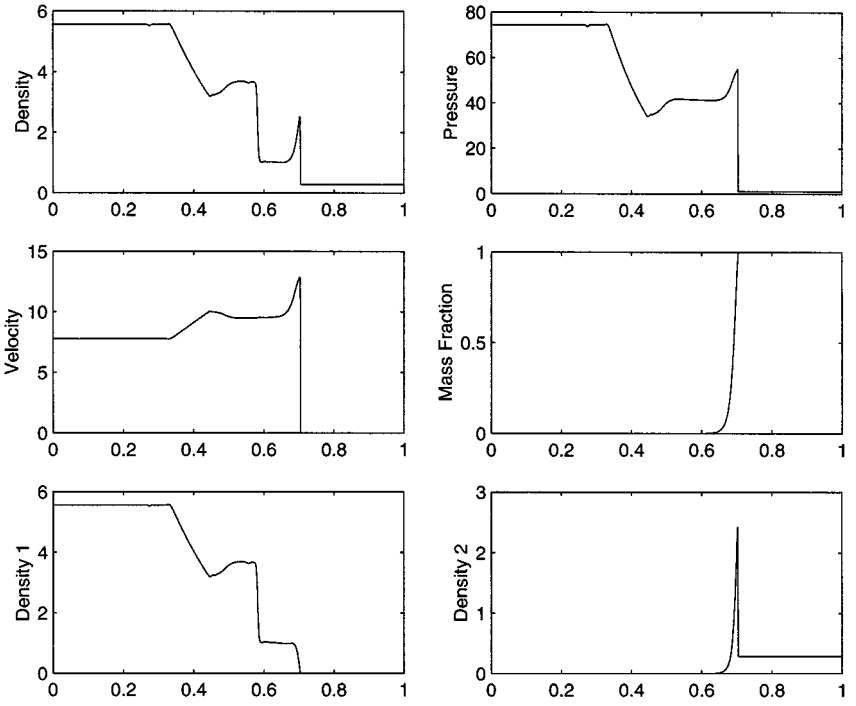

FIG. 12. Strong shock wave ($M = 8.00$) in the air ($\gamma = 1.4$) hits the reactant gas ($\gamma = 1.2$). The cell size is $\Delta x = 1/2000$. The reaction has $E^+ = Q_0 = 50.0$, and $K_0 = 600.0$ (CFL $= 0.5$).

Case (4): Strong shock wave hitting the reactant. We increase the strength of the shock in Case (3) up to $M = 8.0$. The initial condition is

$$W_L = (\rho_L, U_L, P_L, \gamma_L) = (5.565, 7.765, 74.50, 1.4) \quad \text{postshock air}$$
$$W_M = (\rho_M, U_M, P_M, \gamma_M) = (1.0, 0.0, 1.0, 1.4) \quad \text{preshock air}$$
$$W_R = (\rho_R, U_R, P_R, \gamma_R) = (0.287, 0.0, 1.0, 1.2) \quad \text{(reactant)}.$$

Figure 12 shows the numerical results at time $t = 0.05$. From the figure, we observe that after the shock hits the reactant, a ZND solution is obtained.

Case (5): Viscous reactive flow. This case is from [22]. The initial data is a one-dimensional ZND profile in the x direction. The ZND wave connects the left state $\rho_l = 1.731379$, $U_l = 3.015113$, $V_l = 0$, $\rho_l E_l = 130.4736$ by a Chapman–Jouguet detonation with the right state $\rho_r = 1$, $U_r = 0$, $V_R = 0$, $\rho_r E_r = 15$. If no transverse gradient is present in the initial data, the numerical scheme will preserve the one-dimensional ZND profile. Thus, a periodic perturbation is imposed in the y direction in the initial ZND profile, where the initial data $W(x, y, 0)$ is set to $W_{ZND}(x + \Delta x \mathrm{NINT}(\frac{0.05}{\Delta x} \cos(4\pi y)))$, where NINT$(z)$ is the nearest integer to z.

The current test has $Q_0 = E^+ = 50$, $\gamma = 1.2$. The reaction rate K_0 is set to be 10^4. The coefficient of dynamical viscosity μ is set to 10^{-4}. With the above choice of parameters, the half-reaction length $L_{1/2}$ of the inviscid one-dimensional Chapman–Jouguet detonation wave is equal to 0.0285. In our computation, $\Delta x = \Delta y = \frac{1}{800}$ is used. Therefore, there are about 23 points/$L_{1/2}$.

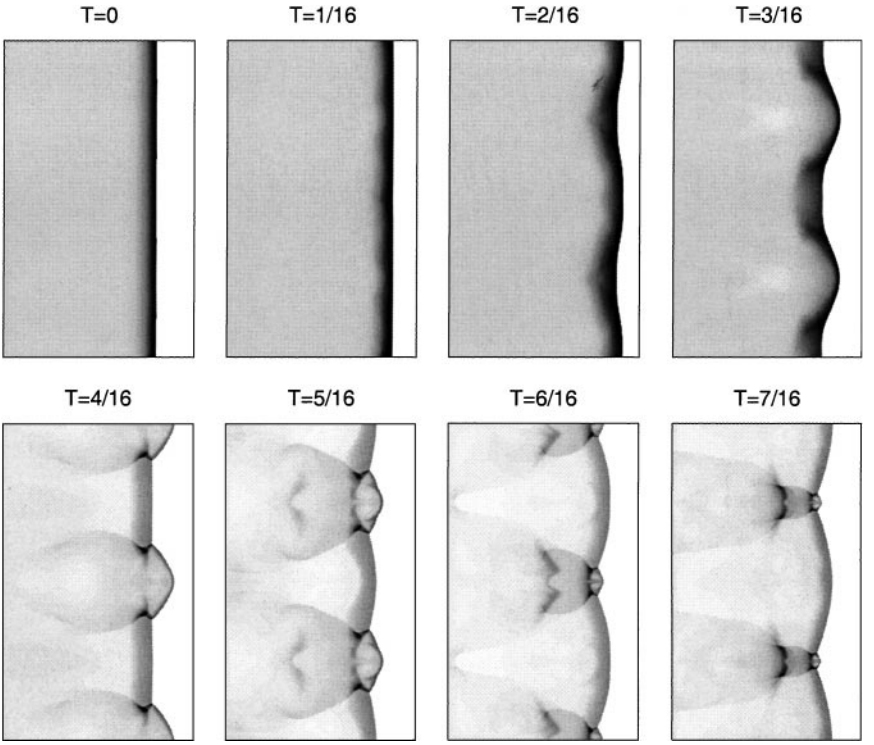

FIG. 13. Sequence of eight snapshots of density distributions starting from time $t = 0$ with a time increment of $\frac{1}{16}$, where $Q_0 = E^+ = 50$, $\gamma = 1.2$, $\Delta x = \Delta y = \frac{1}{800}$, and 23 points/$L_{1/2}$. Shock moves from left to right.

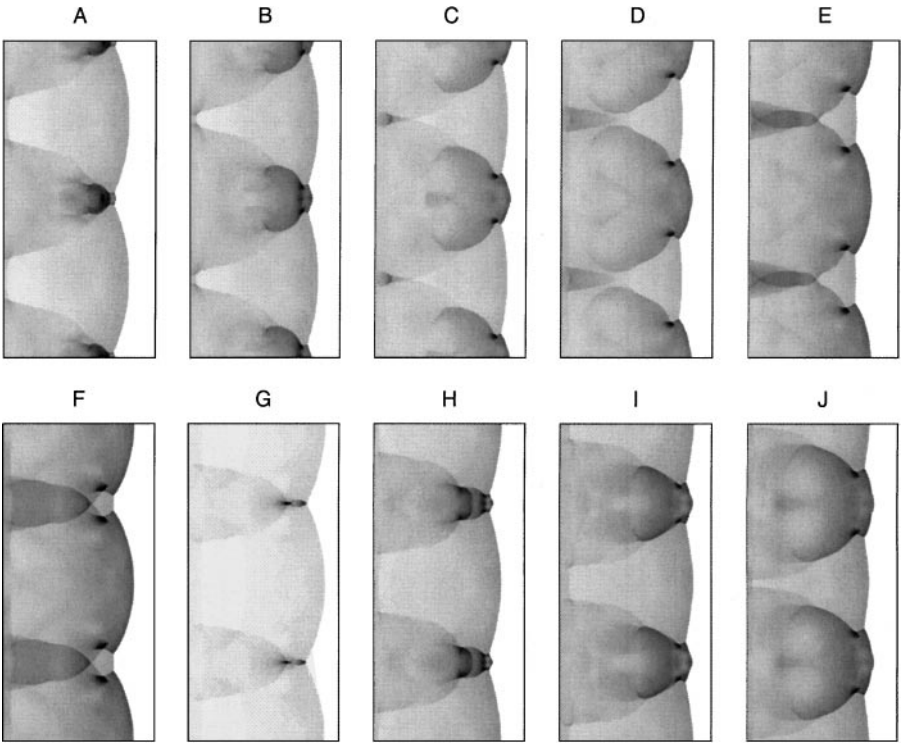

FIG. 14. Sequence of 10 snapshots of pressure distributions starting from time $t = \frac{35}{96}$ with a time increment of $\frac{1}{96}$, where $Q_0 = E^+ = 50$, $\gamma = 1.2$, $\Delta x = \Delta y = \frac{1}{800}$, and 23 points/$L_{1/2}$. Shock moves from left to right.

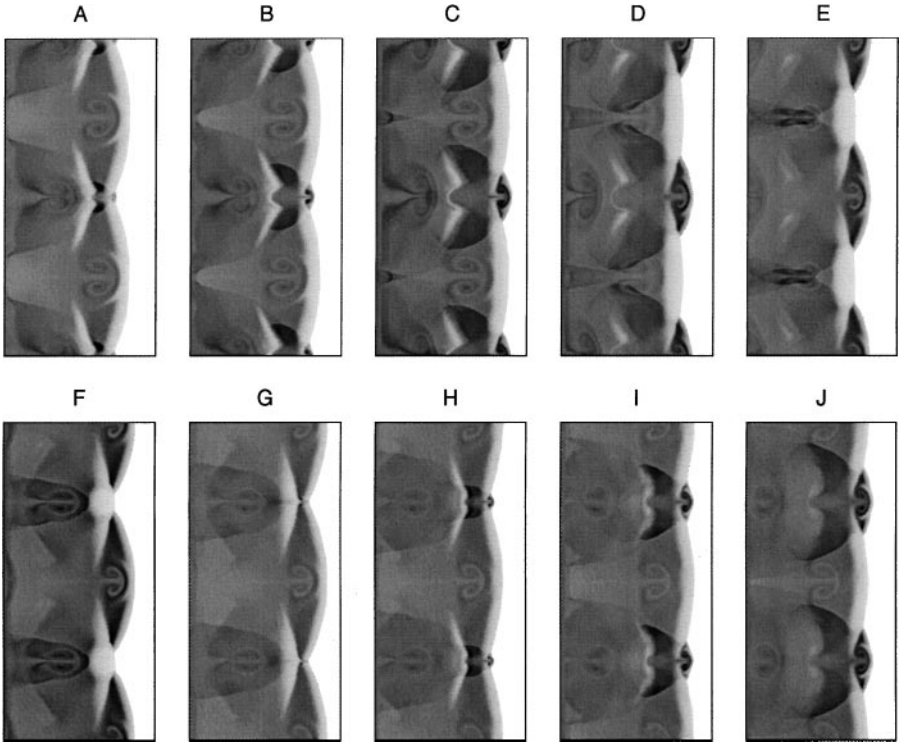

FIG. 15. Sequence of 10 snapshots of temperature distributions starting from time $t = \frac{35}{96}$ with a time increment of $\frac{1}{96}$, where $Q_0 = E^+ = 50$, $\gamma = 1.2$, $\Delta x = \Delta y = \frac{1}{800}$, and 23 points/$L_{1/2}$. Shock moves from left to right.

Based on the analysis in [17], to obtain an accurate solution it is sufficient to use a computational domain $x \in [0, 1.2]$. At the left and the right boundary, we prescribe the left and right state of the initial traveling wave solution. At the lower and upper boundaries, periodic boundary conditions are used.

Figure 13 shows a sequence of snapshots of the density distributions starting from the time $t = 0.0$. Figure 14 is the snapshot of pressure at later times when the shock front has a regular periodic oscillating profile. The first picture is taken at $t = \frac{13}{80}$, which is just after the collision of two triple points. This figure clearly shows the formation of a Mach stem. In the next few snapshots, the movement of triple points along the transverse shock front is clearly captured. A high-pressure spot develops at the location of triple-point intersection. Figure 15 shows the snapshots of the temperature variations. More figures, such as the mass fraction and vorticity, are included in [18].

4. CONCLUSION

In this paper, we have successfully extended the BGK-type gas-kinetic scheme to multidimensional reactive flows. Since each component of the flow is captured individually, mass conservation is preserved for each component in nonreactive multimaterial flow calculations. For reactive flows, the mass exchange between different components and the energy release have been implemented in the current kinetic method. Many numerical test cases validate the current approach in the description of multimaterial and reactive flows.

For example, the unstable and stable material interfaces are captured automatically in the shock–bubble interaction cases.

The success of the kinetic method for the compressible fluid simulation is due to its dissipative mechanism. In the region with smooth flow, the dissipation in the kinetic method is consistent with the Navier–Stokes dissipative term, and the viscosity coefficient is controlled by the collision time. In the unresolved discontinuous region, the BGK scheme still solves the viscous governing equations under the generalized initial condition shown in Fig. 1. We believe that the Godunov method can achieve the same goal once the generalized Riemann solution and explicit viscous fluxes are both implemented in the flow solver. In comparison with Riemann solvers, the advantage of kinetic approaches is probably in their flexibility in the implementation of physics and straightforward construction of numerical fluxes. Further investigation to evaluate and compare the Godunov method and the gas-kinetic schemes is warranted.

ACKNOWLEDGMENTS

The authors are grateful to the reviewers for their comments, which improved the paper. This research was supported in part by the National Aeronautics and Space Administration under NASA Contract NAS1-97046 while the second author was in residence at the Institute for Computer Applications in Science and Engineering (ICASE), NASA Langley Research Center, Hampton, VA. Additional support was provided by Hong Kong Research Grant Council through RGC97/98.HKUST6166/97P.

REFERENCES

1. M. Ben-Artzi, The generalized Riemann problem for reactive flows, *J. Comput. Phys.* **81**, 70 (1989).
2. P. L. Bhatnagar, E. P. Gross, and M. Krook, A model for collision processes in gases. I. Small amplitude processes in charged and neutral one-component systems, *Phys. Rev.* **94**, 511 (1954).
3. A. Bourlioux, *Numerical Study of Unsteady Detonations*, Ph.D. thesis (Princeton University, 1991).
4. A. Bourlioux, J. Majda, and V. Roytburd, Theoretical and numerical structure for unstable one-dimensional detonations, *SIAM J. Appl. Math.* **51**, 303 (1991).
5. A. Bourlioux and J. Majda, Theoretical and numerical structure for unstable detonations, *Phil. Trans. R. Soc. Lond. A* **250**, 29 (1995).
6. S. Chapman and T. G. Cowling, *The Mathematical Theory of Non-uniform Gases* (Cambridge Univ. Press, 1990).
7. P. Colella, A. Majda, and V. Roytburd, Theoretical and numerical structure for reacting shock waves, *SIAM J. Sci. Stat. Comput.* **7**, 1059 (1986).
8. J.-P. Croisille, R. Khanfir, and G. Chanteur, Numerical simulation of the MHD equations by a kinetic-type method, *J. Sci. Comput.* **10**, 81 (1995).
9. S. Engquist and B. Sjögreen, Robust Difference Approximations of Stiff Inviscid Detonation Waves, UCLA CAM Report 91-03 (1991).
10. J. J. Erpenbeck, Stability of idealized one-reaction detonation, *Phys. Fluids* **7**, 684 (1964).
11. R. P. Fedkiw, T. Aslam, B. Merriman, and S. Osher, A non-oscillatory eulerian approach to interfaces in multimaterial flows (the ghost fluid method), *J. Comput. Phys.* **152**, 457 (1999).
12. R. P. Fedkiw, X. D. Liu, and S. Osher, A General Technique for Elimination Spurious Oscillations in Conservative Scheme for Multi-phase and Multi-species Euler Equations, UCLA CAM Report 97-27 (1997).
13. W. Fickett and W. C. Davis, *Detonation* (University of California Press, Berkeley, 1979).
14. W. Fickett and W. W. Wood, Flow calculations for pulsating one-dimensional detonations, *Phys. Fluids* **9**(3), 903 (1966).

15. E. Godlewski and P. A. Raviart, *Numerical Approximation of Hyperbolic Systems of Conservation Laws* (Springer–Verlag, 1996).
16. J. F. Haas and B. Sturtevant, Interactions of weak shock waves with cylindrical and spherical gas inhomogeneities, *J. Fluid Mech.* **181**, 41 (1987).
17. P. Hwang, R. P. Fedkiw, B. Merriman, A. R. Karagozian, and S. J. Osher, Numerical Resolution of Pulsating Detonation, preprint 99-12, UCLA CAM reports (1999).
18. Y. S. Lian, *Two Component Gas-Kinetic Scheme for Reactive Flows*, M.Phil. thesis (Hong Kong University of Science and Technology, 1999).
19. Y. S. Lian and K. Xu, A Gas-Kinetic Scheme for Reactive Flows, ICASE Report 98-55 (1998).
20. K. Kailasanath, E. S. Oran, J. P. Boris, and T. R. Young, Determination of detonation cell size and the role of transverse waves in two-dimension detonations, *Combust. Flame* **61**, 199 (1985).
21. S. Karni, Hybrid multifluid algorithms, *SIAM J. Sci. Comput.* **17**, 1019 (1997).
22. D. Lindström, Numerical Computation of Viscous Detonation Waves in Two Space Dimensions, Report No. 178, Department of Computing, Uppsala University (1996).
23. J. C. Mandal and S. M. Deshpande, Kinetic flux vector splitting for Euler equations, *Comput. Fluids* **23**, 447 (1994).
24. R. W. MacCormack, Algorithmic trends in CFD in the 1990's for aerospace flow field calculations, in M. Y. Hussaini, A. Kumar, and M. D. Salas (Eds.), *Algorithmic Trends in CFD* (Springer–Verlag, 1993).
25. E. S. Oran and J. P. Boris, *Numerical Simulation of Reactive Flow* (Elsevier, 1987).
26. D. I. Pullin, Direct simulation methods for compressible inviscid ideal-gas flow, *J. Comput. Phys.* **34**, 231 (1980).
27. J. J. Quirk, Godunov-Type Schemes Applied to Detonation Flows, ICASE Report No. 93-15 (1993).
28. J. J. Quirk and S. Karni, On the dynamics of a shock bubble interaction, *J. Fluid Mech.* **318**, 129 (1996).
29. M. Short, A. K. Kapila, and J. J. Quirk, The chemical-gas dynamic mechanisms of pulsating detonation wave instability, *Phil. Trans. R. Soc. Lond. A* **357**(1764), 3621 (1999).
30. M. Short and J. J. Quirk, On the nonlinear stability and detonability limit of a detonation wave for a model three-step chain-branching reaction, *J. Fluid Mech.* **339**, 89 (1997).
31. S. Taki and T. Fujiwara, Numerical analysis of two dimensional nonsteady detonations, *AIAA J.* **16**, 73 (1978).
32. E. F. Toro, *Riemann Solvers and Numerical Methods for Fluid Dynamics* (Springer–Verlag, 1999).
33. B. van Leer, Towards the ultimate conservative difference scheme IV, A new approach to numerical convection, *J. Comput. Phys.* **23**, 276 (1977).
34. K. Xu, *Gas-Kinetic Schemes for Unsteady Compressible Flow Simulations*, von Karman Institute for Fluid Dynamics Lecture Series 1998-03 (1998).
35. K. Xu, BGK-based scheme for multicomponent flow calculations, *J. Comput. Phys.* **134**, 122 (1997).
36. K. Xu, A Gas-Kinetic Method for Hyperbolic-elliptic Equations and Its Application in Two phase Fluid Flow, ICASE Report No. 99-31 (1999).
37. K. Xu, Gas-kinetic theory-based flux splitting method for ideal magnetohydrodynamics, *J. Comput. Phys.* **153**, 334 (1999).